A high resolution extreme ultraviolet spectrometer system optimized for harmonic spectroscopy and XUV beam analysis

Martin Wünsche, Silvio Fuchs, Thomas Weber, Jan Nathanael, Johann J. Abel, Julius Reinhard, Felix Wiesner, Uwe Hübner, Slawomir J. Skruszewicz, Gerhard G. Paulus, and Christian Rödel

View Online   **Export Citation**   **CrossMark**

ARTICLES YOU MAY BE INTERESTED IN

Nanopositioning Systems

Modular Motion Control

AFM and NSOM Instruments

Single Molecule Microscopes
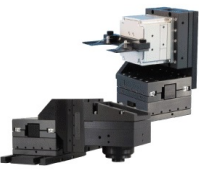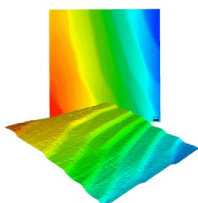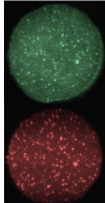
MCL MAD CITY LABS INC.
www.madcitylabs.com

A high resolution extreme ultraviolet spectrometer system optimized for harmonic spectroscopy and XUV beam analysis

View Online   Export Citation   CrossMark

Martin Wünsche,[1,2,3,a] Silvio Fuchs,[1,2,3] Thomas Weber,[1] Jan Nathanael,[1,2] Johann J. Abel,[1] Julius Reinhard,[1]
Felix Wiesner,[1] Uwe Hübner,[4] Slawomir J. Skruszewicz,[1,2] Gerhard G. Paulus,[1,2] and Christian Rödel[1,2]

AFFILIATIONS

[1] Institute of Optics and Quantum Electronics, Friedrich Schiller University Jena, Max-Wien-Platz 1, 07743 Jena, Germany
[2] Helmholtz Institute Jena, Fröbelstieg 3, 07743 Jena, Germany
[3] Indigo Optical Systems GmbH, Jenaische Str. 7, 07747 Jena, Germany
[4] Leibniz Institute of Photonic Technology, Albert-Einstein-Str. 9, 07745 Jena, Germany

[a] martin.wuensche@uni-jena.de

ABSTRACT

We present a modular extreme ultraviolet (XUV) spectrometer system optimized for a broad spectral range of 12–41 nm (30–99 eV) with a high spectral resolution of $\lambda/\Delta\lambda \gtrsim 784 \pm 89$. The spectrometer system has several operation modes for (1) XUV beam inspection, (2) angular spectral analysis, and (3) imaging spectroscopy. These options allow for a versatile use in high harmonic spectroscopy and XUV beam analysis. The high performance of the spectrometer is demonstrated using a novel cross-sectional imaging method called XUV coherence tomography.

I. INTRODUCTION

The advent of extreme ultraviolet (XUV) sources such as free-electron lasers (FLASH[1] FERMI[2]) or laser-driven high harmonic (HHG) sources[3–5] has opened new applications and opportunities in basic research and applied science. In most of the scientific applications, XUV spectrometers with high detection efficiency and resolution are required. For example, XUV spectroscopy has been applied to investigate warm dense hydrogen using Thomson scattering,[6] multi-electron photoionization cross sections,[7] and strong-field laser-atom interactions.[8] The instrument described here has been developed for XUV Coherence Tomography (XCT), a method which has been introduced recently for non-invasive cross-sectional imaging of nanostructures.[9–11] It extends Optical Coherence Tomography (OCT)[12] into the XUV utilizing the short coherence length of broadband XUV radiation. For frequency-domain XCT, the efficiency of the spectrometer

is essential because of the small scattering cross sections in the XUV while the resolution directly corresponds to the maximum depth at which structures can be detected beneath the sample's surface.[13]

Here we focus on an XUV spectrometer that has been developed for the application in XCT using a HHG source[14,15] in the silicon transmission window (30–99 eV, 12–41 nm). For maximum versatility, the instrument can also measure the divergence of the XUV beam and the angularly resolved spectra. This is useful for, e.g., optimization of HHG. In the following, we discuss the requirements for the XUV spectrometer, its technical design, the improved XCT measurements, and the resulting spectrometer resolution.

II. REQUIREMENTS

In XCT, a broad-band XUV beam is reflected at a layered sample. The modulations of the spectral reflectivity are

TABLE I. Comparison of XUV spectrometers regarding resolution.

Spectrometer	Resolution $\lambda/\Delta\lambda$
Transmission grating spectrometer[17]	~100 (at 15 nm)
H + P SXR/EUV spectrometer[18]	~330 (at 20 nm)
HiTRaX[19]	~330 (at 21 nm)
McPherson spectrometer 251MX[20]	~720 (at 20 nm)
T-REXS (this work)	$\gtrsim 784 \pm 89$ (at 20 nm)

analyzed with an XUV spectrometer. To detect a layer buried 1000 nm below the surface, a spectrometer resolution of $\Delta E \sim 0.1$ eV over the entire spectral bandwidth is required. This is equivalent to a resolving power of $R = \lambda/\Delta\lambda = E/\Delta E \sim 600$ at 20 nm. In our previous XCT setup, a transmission grating spectrometer[16] was used that provides a resolution of $\Delta E > 0.4$ eV. Accordingly, higher modulation frequencies and thus deeper lying nanostructures cannot be revealed by XCT using this XUV spectrometer. Additionally, diffraction from the support mesh and the low diffraction efficiency of the transmission grating hampered high-quality XCT measurements.[17] An overview of XUV spectrometers that operate in this wavelength range is shown in Table I. The resolution can be strongly increased[18-20] compared to the transmission grating spectrometer. In this comparison, the highest resolution is obtained by the XUV spectrometer from McPherson (model 251MX). This XUV spectrometer uses a slit that is imaged by a curved reflective grating.

In addition to the high spectral resolution, a highly efficient and sensitive XUV spectrometer is required for XCT due the low reflectivity in the XUV at near-normal incidence which is of the order of $\sim 10^{-5}$. With regard to Table I, the resolution

of the McPherson spectrometer is sufficient for XCT in principle. However, its slit-based concept does not allow focusing along the non-dispersive axis to maximize the sensitivity for XCT. Furthermore, beam alignment and HHG optimization for XCT make an operation mode for online beam inspection desirable. Thus, a new and versatile slit-free XUV spectrometer system is needed that (1) can monitor the XUV beam, (2) can measure the angularly resolved harmonic spectrum, and (3) can measure the XUV radiation with high sensitivity and resolution over the entire bandwidth of 12–41 nm and high efficiency. We therefore developed the Transformable high Resolution high Efficiency XUV Spectrometer (T-REXS) which has three operation modes shown in Fig. 1. In the first mode, the XUV beam is directed via two plane mirrors to the camera detector such that the XUV beam can be measured. In the second mode, the second mirror is replaced by a reflective grating and the angularly resolved spectrum can be measured. In the third mode, the first mirror is replaced by a focusing mirror that images the XUV source onto the detector plane. The highest sensitivity of the spectrometer is obtained in the third mode.

III. SPECTROMETER DESIGN

The basic component of a spectrometer is the dispersive element, which is a grating for the XUV spectral range. The dispersion can be described by the grating equation

$$\sin\beta = \sin\alpha + q \cdot \frac{\lambda}{d}, \tag{1}$$

where α is the incidence angle measured relative to the normal vector of the grating surface. β, q, λ, and d are the deflection angles, the diffraction order, the wavelength, and the grating constant, respectively. For gratings on a concave substrate, wavelengths are focused on the Rowland circle.[21] Better adapted to modern XUV detectors are variable line-spacing (VLS) gratings, which focus the spectrum in a plane (a so-called flat-field).[22,23] The gratings are optimized for a specific geometry, i.e., XUV source size, beam divergence, bandwidth, source-to-grating distance, detector-to-grating distance, angle of incidence, and flat-field plane. Low stray light VLS gratings are commercially available, for example, from Hitachi, Shimadzu, and Horiba. A commonly used VLS grating from Hitachi for 5–20 nm has the following specifications: source-to-grating distance of 237 mm, detector-to-grating distance of 235 mm, incidence angle of $\alpha = 87°$, and groove density of $1/d = 1200$ lines/mm. The VLS grating has a gold coating and is blazed to achieve a diffraction efficiency of >10% in the first diffraction order.[24] According to ray-tracing simulations and the design geometry, a theoretical resolution $R = \lambda/\Delta\lambda \sim 2300$ can be obtained for a source size of 10 μm. In general, an increased source size leads to a reduction in resolution. For the optimization of the XUV spectrometer efficiency and additional focusing in the nondispersive direction, we performed extensive ray-tracing simulations using the ZEMAX software. For a spectrometer geometry that utilizes the VLS grating and a focusing mirror in grazing incidence, the source-to-grating distance must be increased. While the optimization should lead to a high collection
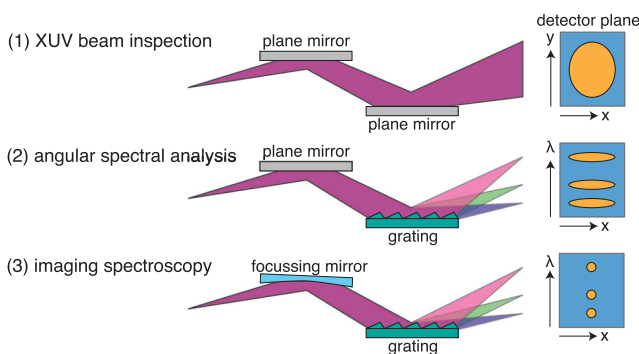

FIG. 1. The spectrometer has three operation modes: (1) XUV beam inspection, (2) angular spectral analysis, and (3) imaging spectroscopy. In the XUV beam inspection mode, two plane mirrors steer the XUV beam to the detector. This operation mode enables assessment of the XUV beam and alignment. In the angular spectral analysis mode, a plane mirror and grating are used. It allows us to measure the spectrum of the XUV beam and the divergence in one direction. In the imaging spectroscopy mode, a cylindrical focusing mirror is used in combination with the grating. It focuses the XUV beam perpendicular to the dispersive axis and images the XUV source in this direction. In this mode, the dispersed XUV radiation is concentrated in the detector plane which leads to a high sensitivity of the spectrometer.

efficiency, the resolution should remain as high as possible. In a first step, we calculated the spectral resolution R for every wavelength in a wide range of the grating-to-source distances z_{grat} of 200–1000 mm, grating angles α_{grat} of 83°–87.5°, and grating-to-camera distances z_{CCD} of 100–400 mm. Based on the results, we calculated the optimum position of the camera, i.e., grating-to-camera distance z_{CCD} and the flat-field angle α_{CCD} with the best resolution over the entire spectrum. The average resolution as a function of the grating distance and grating angle is plotted in Fig. 2. We found that the longer the grating-to-source distance is, the steeper the incidence angle needs to be. In a final step, the position z_{cyl} and curvature r_{cyl} of the collector optics are optimized for the best geometries. A source-to-grating distance of ~850 mm and a grating incidence angle of 84.75° were chosen to adapt the XUV spectrometer to the XCT setup. In this geometry, the flat-field plane is tilted by ~31.6°, the sagittal curvature of the cylindrical mirror is R = 6375 mm, and its incidence angle is 85°. Theoretically, for a point-like XUV source and a detector with infinite spatial resolution, a spectral resolution of 0.003 nm (at 20 nm, 62 eV) corresponding to 0.01 eV could be obtained for this geometry. It is worth noting that the high resolution can also be obtained for considerably smaller source-to-grating distances z_{grat}. The detector should then be tilted less at the position of the flat-field plane. Typically, microchannel plates (MCP) or charge-coupled device (CCD) cameras are used as detectors for XUV spectrometers. The pixel size of XUV cameras is 13.5 μm (CCD chips produced by Teledyne e2v). According to the ray-tracing simulations, the resolution decreases to 0.01 nm or 0.03 eV (at 20 nm, 62 eV) for this pixel size. We also performed ray-tracing simulations with ZEMAX for a source size of 48 μm in the horizontal direction and 135 μm in the vertical direction, which corresponds to our measured XUV focus at the position of the XCT sample. We thus can expect a spectral resolution of $\lambda/\Delta\lambda \sim 700$–900 (at 20 nm) with this XUV spot or XUV source size.

All spectrometer components should be integrated in a vacuum housing with reasonable footprint and weight that can be attached to a vacuum chamber. We constructed a
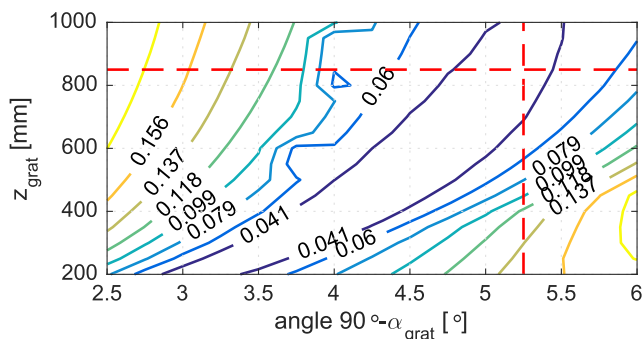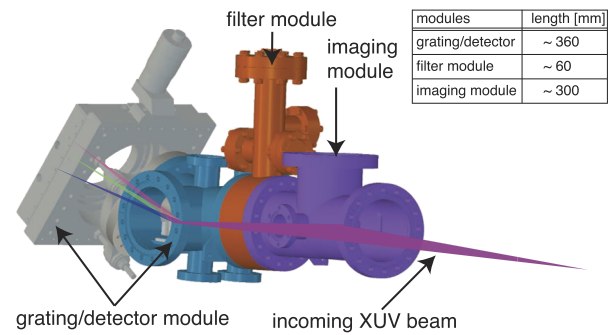

FIG. 3. The XUV spectrometer contains several attachable modules. The essential components of the spectrometer are detector module (gray), which positions the camera in the flat-field plane, and the grating module (blue), which contains the VLS grating and a plane mirror for the beam inspection mode. The filter module (orange) contains thin metal filters that block visible radiation (e.g., laser light in the vacuum chamber). The imaging module (violet) holds a focusing mirror for the imaging spectrometer mode and a plane mirror. The inset shows the lengths of the modules.

compact and versatile vacuum housing; see Fig. 3. By using ConFlat (CF) flanges, the spectrometer vacuum housing can reach an ultra high vacuum (UHV) of around ~10^{-9} mbar. The essential vacuum parts of the spectrometer housing are the camera module, the grating module, the imaging module, and the filter module. The grating and the mirrors can be precisely positioned and aligned using motorized stages. Moreover, it should be possible to switch between the different operation modes without venting. The filter module allows switching between of up to three different metal filters that block optical light. Windows allow visual inspection of the fragile metal filters without venting the spectrometer.

IV. SPECTROMETER USAGE AND OPERATION MODES

The XUV spectrometer is first aligned in the (1) XUV beam inspection mode with a pilot laser. Therefore the two plane mirrors are inserted. The mirrors are coated with boron carbide to provide high reflectivity over the XUV bandwidth. The angle of incidence on the plane mirrors can be aligned using motorized stages. In the XUV beam inspection mode, the XUV beam can be directly investigated using a large CCD camera. The mirror apertures limit the angular acceptance to 6 mrad in the meridional direction and 12 mrad in the sagittal direction.

The second plane mirror can be replaced by the VLS grating using motorized stages. In this mode (2), the spectrum is obtained in the vertical direction, while the beam profile can be measured in the horizontal direction. The resolution of the spectrometer is optimized with a motorized tilt stage. It is worth noting that, in principle, every source-to-grating distance >120 mm can be used when the grating angle is aligned accordingly.

In the third operation mode (3), the first plane mirror is replaced by the focusing mirror such that the XUV beam is focused in the horizontal direction. The focused XUV spectrum leads to a strongly reduced exposure time and a high signal-to-noise ratio. In the following, HHG spectra are

FIG. 2. The average spectral resolution (in eV) within 12–41 nm is plotted for different source-to-grating distances z_{grat} and grating incidence angles α_{grat}. The optimum working point for our XCT setup is indicated with the red dashed cross. The spectral resolution for this geometry is below $\Delta E < 0.04$ eV.

presented which were measured with the XUV spectrometer using the different operation modes.

The harmonics are generated by femtosecond laser pulses, either with a Ti:Sa laser system at 800 nm with 1 kHz, and 2.6 W, or an optical parametric amplifier at 1300 nm with 1 kHz, and 2.4 W (HE-TOPAS, Light Conversion, Lithuania). The latter has the advantage that the driving laser wavelength can be swept automatically, and a quasi-continuous broadband XUV source is achieved at sufficient exposure times.[14]

An angularly resolved HHG spectrum is shown in Fig. 4. Here, 800 nm driving laser pulses with 35 fs were focused by an off-axis parabola (focal length 75 cm) into an argon gas jet. Although the unfocused high-harmonic beam covers almost the full size of the CCD of 512 × 2048 pixels, the divergence of the individual high harmonics can be measured. For example, the harmonic at ~38.7 eV has a FWHM of ~246 pixels, which leads to a divergence (number of pixel × pixel size/CCD-source distance) of 246 × 13.5 μm/1.1 m ~ 3 mrad. By contrast, the harmonic ~69.7 eV has a divergence of ~6.6 mrad. The spherical shape of the grating and the wavelength dependent distances to the detector are taken into account in this measurement.

For measuring faint XUV sources or low signals such as in XCT, the operation mode with the focusing mirror provides the highest sensitivity and signal-to-noise ratio. A high harmonic spectrum recorded with the 1300 nm driver is shown
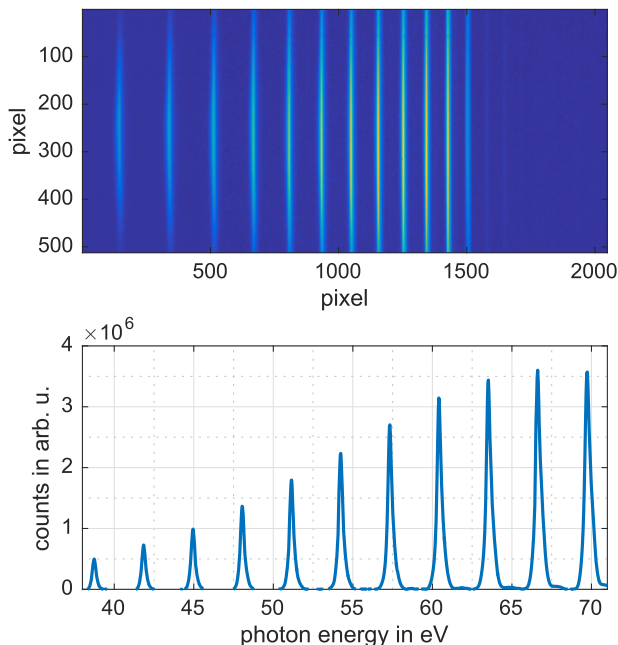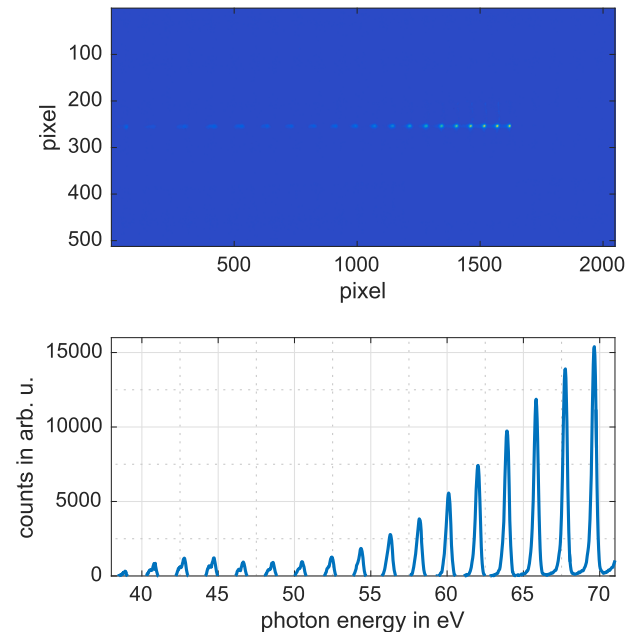

FIG. 5. A HHG spectrum is recorded using the focusing mirror and the 1300 nm driving laser. The XUV beam is focused down to a few pixels on the CCD camera. This leads to a short exposure time of 0.6 s. This operation mode has the highest sensitivity and is typically used for XCT measurements.

in Fig. 5. The XUV beam is focused to a few pixels in the nondispersive direction, while the spectral resolution is not altered.

V. XCT MEASUREMENTS

For the XCT measurements, high harmonics are generated using the 1300 nm driving laser. By sweeping the fundamental laser wavelength (of the HHG process), the time averaged XUV spectrum becomes continuous and smooth.[14] The XUV flux is around ~10^8 photons/(s eV) within 30–70 eV. The XUV beam is focused via a toroidal mirror (focal length 1 m) onto the nanostructured layered sample. Its broadband reflectivity is measured with T-REXS using the focusing operation mode. An XCT signal from a sample which contains two gold layers (230 nm and 330 nm under the surface) and an oxide layer (at 160 nm) is shown in Fig. 6. The exposure time is 5 s. The XUV spectrum is strongly modulated due to the spectral interference of the surface reflection and the buried layers. The depth structure can be retrieved by applying a Fourier-transform on the measured spectrum. The XCT measurement can be improved further by using a spectral phase retrieval algorithm. For details of the XCT depth reconstruction, see the work of Fuchs et al.[15] The depth structure of the sample is shown in Fig. 6. In the XCT postprocessing, the spectral phase retrieval requires a constant spectral sensitivity for the entire bandwidth which was not fulfilled by our previous transmission grating spectrometer.[16] It is worth noting that XCT data measured with T-REXS do not require time

FIG. 4. An angularly resolved high harmonic spectrum is recorded with T-REXS using an 800 nm TiSa laser. The upper image shows the raw data recorded with an Andor Newton DO940 CCD camera. The exposure time is 4 s. The divergence of the high harmonic beam can be investigated using the vertical dimension. The low-order harmonics have a FWHM divergence of 3 mrad, while the higher orders have a divergence of ~6.6 mrad. A spectrum of the HHG beam is obtained by vertical integration or vertical binning (lower image).
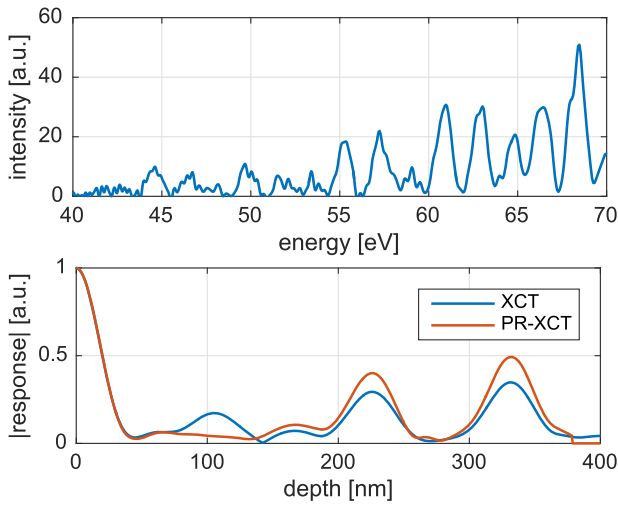
FIG. 6. Upper graph: The plot shows the spectral modulation of the sample measured by the T-REXS. Lower graph: The retrieved depth signal of two gold layers buried under silicon including the autocorrelation artifacts (blue) is shown. The use of the phase retrieval algorithm of XCT removes the autocorrelation artifacts near 100 nm (red). The gold layers are located at 230 nm and 330 nm. An oxide layer is found at 160 nm.

FIG. 7. Principle of the broad bandwidth resolution test: (a) A thin foil is placed in front of a silicon wafer. A small foil-to-surface distance introduces slow spectral oscillations in the spectrometer. (b) Larger foil-to-sample distances lead to faster spectral oscillations. For increasing distances, the resolution $\mathcal{R}(k)$ reduces the ability to resolve the fast oscillations. A scan of the foil-to-surface distance allows a measurement of the FTR.

consuming signal postprocessing which strongly simplifies the XCT data analysis.

VI. RESOLUTION

We consider an XUV spectrum $\mathcal{S}(\lambda)$ or with $k = 2\pi/\lambda$, $\mathcal{S}(k)$ that is measured by using a spectrometer with finite resolution. This can be expressed mathematically by the convolution $\mathcal{S}(k) = \mathcal{F}(k) * \mathcal{R}(k)$ of the initial spectrum $\mathcal{F}(k)$ and a function $\mathcal{R}(k) \propto \exp\left(-4\ln 2(k-k_0)^2/(\Delta k)^2\right)$ that describes the resolution Δk. When a Fourier-transform (FT) is applied, the convolution in spectral domain becomes a multiplication in spatial domain, i.e., $\mathrm{FT}[\mathcal{S}(k)] = \mathrm{FT}[\mathcal{F}(k)] \cdot \mathrm{FT}[\mathcal{R}(k)]$. The Fourier-transform of the resolution function is also a Gaussian, which is referred to as the Fourier-transform resolution (FTR = $|\mathrm{FT}[\mathcal{R}(k)]|$). The width of the resolution function and the width of the FTR are connected through a relation $\Delta k \cdot \Delta x = const$. In the context of spectral interferometry,[25–27] slow spectral oscillations in $\mathcal{S}(\lambda)$ or $\mathcal{S}(k)$ correspond to small distances in the spatial domain and fast spectral oscillations correspond to large distances. As a consequence, fast oscillating spectral features require high spectral resolution.

In the XCT technique, we measure spectral modulations over a large bandwidth whereby higher modulation frequencies in the spectrum correspond to deeper layers of a sample. These spectral interferograms can be exploited for a FTR resolution test.

For spectrometers with infinite resolution, the FTR would be a constant, FTR = 1. Due to the decreasing diffraction angle for shorter wavelengths, the spectrum is not equidistant in the detector plane. Accordingly, the spectrometer resolution effectively limits the bandwidth and thus the maximum depth. In addition, the finite spectrometer resolution reduces the
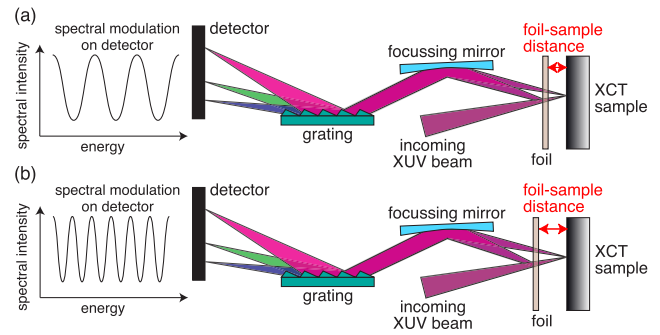
modulation depth of the spectral modulation. The contrast of the XCT depth structure is thus lowered.

For determining the resolution using the FTR, a nm-thin foil (30 nm Si_3N_4) is placed in front of a silicon wafer. The foil-to-surface distance can be varied using piezoactuators. A continuous, smooth XUV spectrum is used for this measurement.[14] A scan of the foil distance is performed while measuring the spectral interferogram with the T-REXS. We thus obtain a measurement of the FTR. The experimental setup for the resolution is shown in Fig. 7. Before we discuss the result of the measurement, we first model the FTR; see Fig. 8. We assume an FTR width of $\Delta x = 2\,\mu$m,

$$\mathrm{FTR} \propto \exp\left(-4\ln 2\frac{x^2}{(\Delta x)^2}\right) \quad . \tag{2}$$

The resolution in spectral domain is calculated via a Fourier transform,

$$\overline{\Delta E} = \hbar c \Delta k = \hbar c \frac{4\ln 2}{\pi \Delta x}. \tag{3}$$
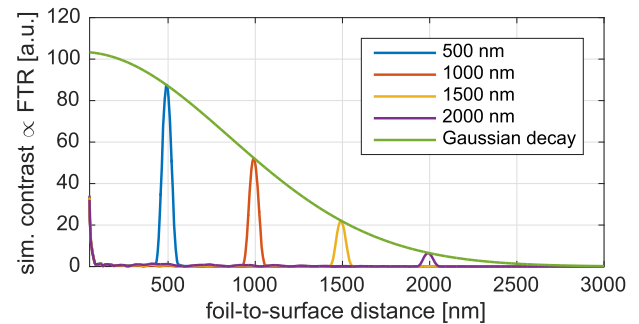

FIG. 8. A simulated FTR and the decay of the simulated contrast for different foil-to-surface distances are shown (500, 1000, 1500, and 2000 nm). Due to the finite resolution of a spectrometer, the signal decreases with increasing distance. The FWHM width $\Delta x = 2\,\mu$m of the FTR corresponds to a resolution of $\overline{\Delta E} = 0.087$ eV.
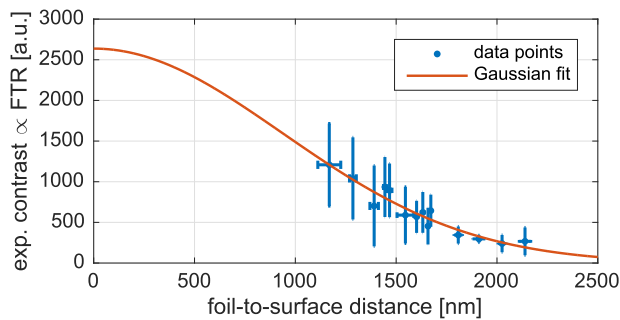
FIG. 9. Measurement of the FTR with T-REXS decreases over the depth. The foil-to-surface distance was scanned in the range of 1–2 μm. Every data point is an average of 10 exposures. The error bars are represented by the standard deviation. The FWHM of the FTR is found to be Δx = 2.2 ± 0.2 μm or ΔE = 0.080 ± 0.009 eV which corresponds to a resolving power $R = k/\overline{\Delta k} = \lambda/\Delta\lambda = E/\overline{\Delta E} \gtrsim 784 \pm 89$ (at 62 eV, 20 nm).

For the present example, this leads to a resolution of $\overline{\Delta E}$ = 0.087 eV in a bandwidth of 30–70 eV. We performed the measurement of the FTR and varied the foil-to-surface distance in a range of 1–2 μm. Shorter distances could not be reached due to mechanical constraints. For each distance, a broad spectrum in the range of 30–70 eV is recorded with the T-REXS. The resulting FTR measurement is shown in Fig. 9. Each point in the graph represents the average of 10 exposures. The error bars are obtained by the standard deviation. Due to fluctuations in laser power and vibration of the nm-thin foil, the error bars are relatively large. The noise level is given by the residual modulations of the harmonic spectrum. We achieved a signal-to-noise ratio which is better than 1.88. A Gaussian curve is fitted to the data points providing a FWHM width of Δx = 2.2 ± 0.2 μm. This corresponds to a resolution of $\overline{\Delta E}$ = 0.080 ± 0.009 eV and a resolving power of $R = E/\overline{\Delta E} = \lambda/\Delta\lambda \gtrsim 784 \pm 89$. Here, we used 62 eV (20 nm) for the calculation of the resolving power. The error of the resolution measurement is determined by the 95% confidence interval of the Gaussian fit. The measured resolution is in good agreement with the expectations from ray-tracing simulations assuming an XUV source size of approximately 100 μm.

VII. CONCLUSION

We presented a high-resolution high-efficiency XUV spectrometer that is optimized for the characterization of HHG beams and the cross-sectional imaging technique XCT. An approach for determining the resolution over a large bandwidth has been presented that is based on Fourier-transform spectroscopy. The measurements make use of a nm-thin freestanding foil such that spectral modulations are introduced in dependence of different foil positions. The resolving power was estimated at $\lambda/\Delta\lambda$ = 784 ± 89 at 20 nm for an extended XUV source of around 100 μm. However, positioning the foil is challenging and thus results in relatively large error bars. On the other hand, raytracing simulations indicate that the determined resolution can be expected at this XUV source

size. Due to the high performance over a large spectral range in the XUV spectral range, the spectrometer is highly suited for high harmonic spectroscopy and spectral interferometry in the XUV spectral range. Motorized stages and vacuum manipulators allow for switching the different operation modes and for alignment of the XUV spectrometer in vacuum. The spectrum and the beaming of the XUV radiation can be studied by three different operation modes: (1) measurement of the direct XUV beam, (2) measurement of the angularly resolved XUV spectrum, and (3) imaging spectroscopy using a focusing mirror. In the third operation mode, the highest sensitivity and signal-to-noise ratio are achieved. This is particularly important for low signal applications such as XCT. Respective measurements performed with T-REXS demonstrate its high performance and considerable improvements in comparison with the previously used spectrometer.

REFERENCES

[1]W. Ackermann, G. Asova, V. Ayvazyan, A. Azima, N. Baboi, J. Bähr, V. Balandin, B. Beutner, A. Brandt, A. Bolzmann, R. Brinkmann, O. I. Brovko, M. Castellano, P. Castro, L. Catani, E. Chiadroni, S. Choroba, A. Cianchi, J. T. Costello, D. Cubaynes, J. Dardis, W. Decking, H. Delsim-Hashemi, A. Delserieys, G. Di Pirro, M. Dohlus, S. Düsterer, A. Eckhardt, H. T. Edwards, B. Faatz, J. Feldhaus, K. Flöttmann, J. Frisch, L. Fröhlich, T. Garvey, U. Gensch, C. Gerth, M. Görler, N. Golubeva, H.-J. Grabosch, M. Grecki, O. Grimm, K. Hacker, U. Hahn, J. H. Han, K. Honkavaara, T. Hott, M. Hüning, Y. Ivanisenko, E. Jaeschke, W. Jalmuzna, T. Jezynski, R. Kammering, V. Katalev, K. Kavanagh, E. T. Kennedy, S. Khodyachykh, K. Klose, V. Kocharyan, M. Körfer, M. Kollewe, W. Koprek, S. Korepanov, D. Kostin, M. Krassilnikov, G. Kube, M. Kuhlmann, C. L. S. Lewis, L. Lilje, T. Limberg, D. Lipka, F. Löhl, H. Luna, M. Luong, M. Martins, M. Meyer, P. Michelato, V. Miltchev, W. D. Möller, L. Monaco, W. F. O. Müller, O. Napieralski, O. Napoly, P. Nicolosi, D. Nölle, T. Nuñez, A. Oppelt, C. Pagani, R. Paparella, N. Pchalek, J. Pedregosa-Gutierrez, B. Petersen, B. Petrosyan, G. Petrosyan, L. Petrosyan, J. Pflüger, E. Plönjes, L. Poletto, K. Pozniak, E. Prat, D. Proch, P. Pucyk, P. Radcliffe, H. Redlin, K. Rehlich, M. Richter, M. Roehrs, J. Roensch, R. Romaniuk, M. Ross, J. Rossbach, V. Rybnikov, M. Sachwitz, E. L. Saldin, W. Sandner, H. Schlarb, B. Schmidt, M. Schmitz, P. Schmüser, J. R. Schneider, E. A. Schneidmiller, S. Schnepp, S. Schreiber, M. Seidel, D. Sertore, A. V. Shabunov, C. Simon, S. Simrock, E. Sombrowski, A. A. Sorokin, P. Spanknebel, R. Spesyvtsev, L. Staykov, B. Steffen, F. Stephan, F. Stulle, H. Thom, K. Tiedtke, M. Tischer, S. Toleikis, R. Treusch, D. Trines, I. Tsakov, E. Vogel, T. Weiland, H. Weise, M. Wellhöfer, M. Wendt, I. Will, A. Winter, K. Wittenburg, W. Wurth, P. Yeates, M. V. Yurkov, I. Zagorodnov, and K. Zapfe, Nat. Photonics **1**, 336 (2007).

[2]E. Allaria, R. Appio, L. Badano, W. Barletta, S. Bassanese, S. Biedron, A. Borga, E. Busetto, D. Castronovo, P. Cinquegrana, S. Cleva, D. Cocco, M. Cornacchia, P. Craievich, I. Cudin, G. D'Auria, M. Dal Forno, M. Danailov, R. De Monte, G. De Ninno, P. Delgiusto, A. Demidovich, S. Di Mitri, B. Diviacco, A. Fabris, R. Fabris, W. Fawley, M. Ferianis, E. Ferrari, S. Ferry, L. Froehlich, P. Furlan, G. Gaio, F. Gelmetti, L. Giannessi, M. Giannini,

R. Gobessi, R. Ivanov, E. Karantzoulis, M. Lonza, A. Lutman, B. Mahieu, M. Milloch, S. Milton, M. Musardo, I. Nikolov, S. Noe, F. Parmigiani, G. Penco, M. Petronio, L. Pivetta, M. Predonzani, F. Rossi, L. Rumiz, A. Salom, C. Scafuri, C. Serpico, P. Sigalotti, S. Spampinati, C. Spezzani, M. Svandrlik, C. Svetina, S. Tazzari, M. Trovo, R. Umer, A. Vascotto, M. Veronese, R. Visintini, M. Zaccaria, D. Zangrando, and M. Zangrando, Nat. Photonics **6**, 699 (2012).

[3]T. Popmintchev, M.-C. Chen, A. Bahabad, M. Gerrity, P. Sidorenko, O. Cohen, I. P. Christov, M. M. Murnane, and H. C. Kapteyn, Proc. Natl. Acad. Sci. U. S. A. **106**, 10516 (2009).

[4]C. M. Heyl, J. Güdde, A. L'Huillier, and U. Höfer, J. Phys. B: At., Mol. Opt. Phys. **45**, 074020 (2012).

[5]R. Klas, S. Demmler, M. Tschernajew, S. Hädrich, Y. Shamir, A. Tünnermann, J. Rothhardt, and J. Limpert, Optica **3**, 1167 (2016).

[6]R. R. Fäustlin, T. Bornath, T. Döppner, S. Düsterer, E. Förster, C. Fortmann, S. H. Glenzer, S. Göde, G. Gregori, R. Irsig, T. Laarmann, H. J. Lee, B. Li, K.-H. Meiwes-Broer, J. Mithen, B. Nagler, A. Przystawik, H. Redlin, R. Redmer, H. Reinholz, G. Röpke, F. Tavella, R. Thiele, J. Tiggesbäumker, S. Toleikis, I. Uschmann, S. M. Vinko, T. Whitcher, U. Zastrau, B. Ziaja, and T. Tschentscher, Phys. Rev. Lett. **104**, 125002 (2010).

[7]A. D. Shiner, B. E. Schmidt, C. Trallero-Herrero, H. J. Wörner, S. Patchkovskii, P. B. Corkum, J.-C. Kieffer, F. Légaré, and D. M. Villeneuve, Nat. Phys. **7**, 464 (2011).

[8]K. J. Schafer, M. B. Gaarde, A. Heinrich, J. Biegert, and U. Keller, Phys. Rev. Lett. **92**, 023003 (2004).

[9]G. G. Paulus and C. Rödel, U.S. patent 7656538 (27 February 2008).

[10]S. Fuchs, C. Rödel, A. Blinne, U. Zastrau, M. Wünsche, V. Hilbert, L. Glaser, J. Viefhaus, E. Frumker, P. Corkum, E. Förster, and G. G. Paulus, Sci. Rep. **6**, 20658 (2016).

[11]P. Wachulak, A. Bartnik, and H. Fiedorowicz, Sci. Rep. **8**, 8494 (2018).

[12]D. Huang, E. Swanson, C. Lin, J. Schuman, W. Stinson, W. Chang, M. Hee, T. Flotte, K. Gregory, C. Puliafito, and A. Et, Science **254**, 1178 (1991); e-print arXiv:9809069v1 [arXiv:gr-qc].

[13]S. Fuchs, A. Blinne, C. Rödel, U. Zastrau, V. Hilbert, M. Wünsche, J. Bierbach, E. Frumker, E. Förster, and G. G. Paulus, Appl. Phys. B **106**, 789 (2012).

[14]M. Wünsche, S. Fuchs, S. Aull, J. Nathanael, M. Möller, C. Rödel, and G. G. Paulus, Opt. Express **25**, 6936 (2017).

[15]S. Fuchs, M. Wünsche, J. Nathanael, J. J. Abel, C. Rödel, J. Biedermann, J. Reinhard, U. Hübner, and G. G. Paulus, Optica **4**, 903 (2017).

[16]J. Jasny, U. Teubner, W. Theobald, C. Wülker, J. Bergmann, and F. P. Schäfer, Rev. Sci. Instrum. **65**, 1631 (1994).

[17]S. Fuchs, C. Rödel, M. Krebs, S. Hädrich, J. Bierbach, A. E. Paz, S. Kuschel, M. Wünsche, V. Hilbert, U. Zastrau, E. Förster, J. Limpert, and G. G. Paulus, Rev. Sci. Instrum. **84**, 023101 (2013).

[18]R. Hörlein and H+P SPECTROSCOPY, "XUV spectrograph," https://www.hp-spectroscopy.com/prodxuv, 2013, accessed on 2018-02-01.

[19]R. R. Fäustlin, U. Zastrau, S. Toleikis, I. Uschmann, E. Förster, and T. Tschentscher, J. Instrum. **5**, P02004 (2010).

[20]McPherson, "251MX–Aberration corrected flat field," https://mcphersoninc.com/pdf/251MX.pdf, 2018, accessed on 2018-03-13.

[21]C. Palmer, *Diffraction Grating Handbook*, 7th ed. (Newport Corporation, 2014).

[22]T. Kita, T. Harada, N. Nakano, and H. Kuroda, Appl. Opt. **22**, 512 (1983).

[23]N. Nakano, H. Kuroda, T. Kita, and T. Harada, Appl. Opt. **23**, 2386 (1984).

[24]J. Edelstein, M. C. Hettrick, S. Mrowka, P. Jelinsky, and C. Martin, Appl. Opt. **23**, 3267_1 (1984).

[25]P. Salières, L. Le Déroff, T. Auguste, P. Monot, P. D'Oliveira, D. Campo, J.-F. Hergott, H. Merdji, and B. Carré, Phys. Rev. Lett. **83**, 5483 (1999).

[26]Y. Mairesse, O. Gobert, P. Breger, H. Merdji, P. Meynadier, P. Monchicourt, M. Perdrix, P. Salières, and B. Carré, Phys. Rev. Lett. **94**, 173903 (2005).

[27]N. de Oliveira, M. Roudjane, D. Joyeux, D. Phalippou, J.-C. Rodier, and L. Nahon, Nat. Photonics **5**, 149 (2011).